JGR Space Physics

RESEARCH ARTICLE
10.1029/2023JA031301

Key Points:

- Solar wind protons and planetary protons are analyzed separately using the updated magnetohydrodynamic model
- Planetary proton loss is estimated to be larger than heavy ion loss, but 1–2 orders less than neutral hydrogen loss
- The effects of impact ionization and H-O charge exchange reactions are quantified

Supporting Information:

Supporting Information may be found in the online version of this article.

Correspondence to:

Y. Ma,
yingjuan@igpp.ucla.edu

Citation:

Sun, W., Ma, Y., Russell, C. T., Luhmann, J., Nagy, A., & Brain, D. (2023). 5-Species MHD study of Martian proton loss and source. *Journal of Geophysical Research: Space Physics*, *128*, e2023JA031301. https://doi.org/10.1029/2023JA031301

Received 8 JAN 2023
Accepted 22 MAR 2023

5-Species MHD Study of Martian Proton Loss and Source

Wenyi Sun[1], Yingjuan Ma[1], Christopher T. Russell[1], Janet Luhmann[2], Andrew Nagy[3], and David Brain[4]

[1]University of Califonial Los Angeles, Los Angeles, CA, USA, [2]University of California, Berkeley, Berkeley, CA, USA, [3]University of Michigan, Ann Arbor, MI, USA, [4]University of Colorado Boulder, Boulder, CO, USA

Abstract Although photochemistry-enabled escape of oxygen is a dominant atmospheric loss process at Mars today, ion outflow plays an essential role in the long-term evolution of Mars' atmosphere. Apart from heavy planetary ions such as O^+, O_2^+, and CO_2^+, the loss of planetary protons is also important because it could be related to water loss. To study planetary proton loss due to solar wind interaction, we improve the 4-species (O^+, O_2^+, CO_2^+, and H^+) single-fluid magnetohydrodynamic (MHD) model of Mars, to a 5-species (separating planetary protons and solar wind protons) MHD model so that the two types of protons can be tracked separately. The global distributions of solar wind protons and planetary ions at low altitudes are investigated. The calculated planetary proton escape rates are larger than heavy ion loss rates and solar wind proton inflows for both solar maximum and minimum conditions. Planetary proton escape rates are 1–2 orders less than neutral hydrogen loss, suggesting that planetary protons could contribute to no >10% of the hydrogen loss under current conditions. By comparing normal cases with cases for which H-O charge exchange reactions or electron impact ionizations are switched off, we find that H-O charge exchange mainly affects densities at low altitudes, while impact ionizations exert great influence on escape rates at high altitudes. The overall results suggest the specific treatment of proton origins in models of Mars atmosphere escape provides better insight into the contributing processes, and should be included in future studies focusing on water's fate.

Plain Language Summary It is commonly believed that Mars has lost most of its atmosphere. While there are many works on the escape rates of heavy ions such as O^+, O_2^+, and CO_2^+, there are few studying proton loss which is also important due to its relation to the loss of water. We separate the protons from the solar wind and protons originating in the planetary atmosphere, so that the 4-species (O^+, O_2^+, CO_2^+, and H^+) single-fluid magnetohydrodynamic (MHD) model is improved to a 5-species (separating planetary protons and solar wind protons) MHD model. The global distributions of solar wind protons and planetary ions at low altitudes are discussed. The calculated escape rates suggest that planetary proton loss is important compared with heavy ion loss and solar wind proton inflow, even though planetary proton loss is no >10% of previously estimated atomic hydrogen loss. We investigate the effects of two types of reactions where protons are involved: H-O charge exchange and electron impact ionization. We find that impact ionization is important at high altitudes therefore also important for escape rates, while H-O charge exchange mainly exerts influence at low altitudes. The total integrations of chemical reactions indicate their relative importance.

1. Introduction

Substantial evidence suggests that the Martian atmosphere has changed dramatically over its history. Its formerly thick and moist atmosphere has now become a thin and dry atmosphere dominated by CO_2 (Jakosky & Phillips, 2001). The striking differences between ancient and present Martian atmospheres indicate that atmospheric escape may have played a significant role in Mars climate evolution.

Particular interest exists regarding the loss mechanisms affecting water. Although much attention has been focused on the loss of its oxygen constituent, the pathways for hydrogen loss are also key to understanding its evolution (e.g., Stone et al., 2020). Atomic hydrogen in the Martian upper atmosphere is produced by the dissociation of H_2, which is converted from H_2O (Stone et al., 2020). The total H escape rate derived from Mars Atmosphere and Volatile EvolutioN (MAVEN) measurements varies between 1×10^{26} s^{-1} and 1.1×10^{27} s^{-1} (Jakosky et al., 2018).

In contrast to the escape of neutral atomic hydrogen, ion escape is strongly influenced by the solar wind interaction, where solar conditions and planetary magnetic field are important factors. The solar wind interaction can

accelerate ions to escape velocity via multiple processes, including the convection electric field which controls ion pickup (Dubinin et al., 2006), $J \times B$ acceleration in the tail region (Dubinin et al., 1993) which is the major cause of ion escape in magnetohydrodynamic (MHD), wave-driven acceleration (Ergun et al., 2006), etc. Mars does not have an intrinsic global magnetic field similar to Earth, but instead has local crustal magnetic anomalies (Acuña et al., 1999). As a result, Mars is in a more complex plasma environment than other unmagnetized bodies such as Venus. The crustal field influences the ion density in the ionosphere and the interaction between ionosphere and solar wind, therefore influencing the ion escape. These effects have been studied with in situ observations (e.g., Dubinin et al., 2020) and numerical models (e.g., Dong, Bougher, et al., 2015; Fang et al., 2015; Ma et al., 2014), but remain to be fully understood (Gunell et al., 2018).

Plasma interaction processes around Mars have been observed by many missions such as Phobos-2 (Lundin et al., 1990), Mars Express (MEX; Barabash et al., 2007) and more recently, by the MAVEN mission (Jakosky et al., 2015). Even though the planetary proton loss rate is hard to determine, heavy ion escape rates have been studied for decades. For example, with Phobos-2 data, Lundin et al. (1990) estimated an O^+ escape rate of $\sim 3 \times 10^{25}$ ions/s. With MEX data, Ramstad et al. (2015) showed heavy ion escape rates varying roughly in a range of $1–6 \times 10^{24}$ ions/s. With MAVEN data, Brain et al. (2015) placed a lower limit of 2.8×10^{24} ions/s on the heavy ion escape rate and showed the spatial distribution of heavy ion fluxes. Measured heavy ion escape rates show great discrepancies partially because of different energy ranges and solar conditions.

Many global models have been developed to study the interaction and quantify the ion loss rates. Different types of models all show consistency with measurements to some extent. For example, Harnett and Winglee (2006) utilized a multifluid MHD model to determine O_2^+ outflow for diverse solar wind conditions and found that the result for quiet solar wind condition was comparable to that of Phobos-s measurements. By incorporating background magnetic and convection electrical fields from an MHD model into their test particle model, Fang et al. (2008) calculated the escape rate of pickup O^+ which fell within the limits of earlier measurements. Brecht and Ledvina (2010) studied the oxygen ion loss using a hybrid model in the context of the loss of water. Ma et al. (2015) compared the simulation results of a time-dependent multispecies single-fluid MHD model with the MAVEN observations along the spacecraft orbit, with bow shock location, plasma conditions inside the magnetosheath region and ion densities agreeing well with the data. Dong, Ma, et al. (2015) used a steady-state multifluid MHD model to reproduce the features of an ICME event. Ledvina et al. (2017) demonstrated that the heavy ion escape rate and distribution calculated from their hybrid model agree with observations.

However, previous modeling works have mainly focused on heavy ion escape rates. Few models focus on proton escape, which could be related to the loss of water. Here, we investigate the behavior of protons in the near-Mars region with a 5-species MHD model, in which the density of solar wind protons and planetary protons are tracked separately. With this model, the proton flux originating from the planetary ionosphere can be calculated, not mixed with solar wind protons as before. The description and simulation setup of the model are given in Section 2. Results from the model are presented and discussed in Section 3. The paper ends with a brief conclusion.

2. Model Description

A multispecies single-fluid MHD model of Mars is used for the steady-state calculation employing the University of Michigan BATS-R-US code (Powell et al., 1999; Tóth et al., 2012). We solve a set of ideal MHD equations (Ma et al., 2004), which consists of multiple continuity, one momentum, the magnetic induction, and one energy equations. Only one momentum and energy equations are solved here, because it is assumed that all ion species have the same velocity and temperature in the single-fluid MHD model. There are five ion species considered in our calculation: H^+_p for planetary protons, H^+_{sw} for solar wind protons, and heavy ions O^+, O_2^+, CO_2^+. Table 1 lists the chemical reactions included in this study, which can be sorted into five categories: photoionization, impact ionization, H-O charge exchange, O-CO_2 charge exchange, and dissociative recombination. To distinguish solar wind protons and planetary protons, the reactions where protons perform as reactants are calculated separately, while all the protons produced by hydrogen in Martian atmosphere are marked as planetary protons. The main loss pathways of protons are H^+_p escape to space and neutralization by charge exchange. The 4-species cases are used for comparison and validation of the 5-species model. In Sections 3.2 and 3.3, in order to quantify the effects of different types of reactions contributing to H^+_p loss and source, we run two sets of special cases besides normal cases: 5-species without H-O charge exchange (HOCX) and 5-species without impact ionization

Table 1
List of Chemical Reactions Considered in Previously Used 4-Species and the Improved 5-Species MHD Models

Reaction	4-Species	5-Species
Photoionization	$H + h\nu \rightarrow H^+ + e$	$H + h\nu \rightarrow H^+_p + e$
	$O + h\nu \rightarrow O^+ + e$	Same as 4-species
	$CO_2 + h\nu \rightarrow CO_2^+ + e$	
Impact ionization	$H + e^* \rightarrow H^+ + 2e$	$H + e^* \rightarrow H^+_p + 2e$
	$O + e^* \rightarrow O^+ + 2e$	Same as 4-species
O-CO_2 charge exchange	$CO_2^+ + O \rightarrow O_2^+ + CO$	Same as 4-species
	$CO_2^+ + O \rightarrow O^+ + CO_2$	
	$O^+ + CO_2 \rightarrow O_2^+ + CO$	
H-O charge exchange	$O^+ + H \rightarrow H^+ + O$	$O^+ + H \rightarrow H^+_p + O$
	$H^+ + O \rightarrow O^+ + H$	$H^+_{sw} + O \rightarrow O^+ + H$
		$H^+_p + O \rightarrow O^+ + H$
Dissociative recombination	$O_2^+ + e \rightarrow O + O$	Same as 4-species
	$CO_2^+ + e \rightarrow CO + O$	

Note. The subscripts p indicates a planetary proton and subscript sw indicates solar wind origins.

(ImpIon). Given that solar activity condition influences neutral atmosphere and ionization rates greatly, every set of cases is conducted with solar max and solar min conditions, respectively.

The model calculations are performed in the Mars-centered Solar Orbital (MSO) coordinate system: the x-axis points from Mars to the Sun, the y-axis points antiparallel to Mars' orbital velocity, and the z-axis completes the right-handed coordinate system. We choose a computational domain of $-24R_M < x < 12R_M$, $-16R_M < y$, and $z < 16R_M$, where R_M is the radius of Mars (3,396 km). The domain is large enough so that the near-Mars region of our interest is not influenced by the outer boundary conditions. A nonuniform, spherical grid structure is used with the radial resolution varying from 5 km at the inner boundary (100-km altitude) to ~2,100 km near the outer boundary. The angular resolution is 3° in both longitudinal and latitudinal directions. The 1-D neutral atmospheric profiles and reaction rates are the same as in Ma et al. (2004), except that hydrogen density profiles above 200 km are updated based on Chaufray et al. (2015). The updated and previous hydrogen density profiles are shown in Figure 1. In this work, the hydrogen profiles are assumed to be isothermal, with gravity change in altitude considered. The temperatures are estimated based on the seasonal-averaged dayside values, which are marked as dots in Figure 2. The H density profiles stop at $3R_M$ (corresponding to 6,792 km in Figure 2) because the ion chemistry beyond that altitude is neglected. In our model, the column density of H above the bow shock is 4.11×10^{12} cm^{-2} during solar maximum and 2.35×10^{12} cm^{-2} during solar minimum. These values fall within the same range as those obtained from MAVEN observations, provided that the observations are not taken during the Martian southern summer solstice, when the column density is much higher than the normal level (Halekas, 2017; Halekas & McFadden, 2021). Following Ma et al. (2004), the 60-order spherical harmonic model by Arkani-Hamed (2001) is adopted for the crustal magnetic field. In this study, all cases are set with the strong crustal field on the dayside except one special case in Section 3.1 without the crustal field to examine the effects of the crustal field on the distribution of ions. Solar wind parameters are set to be typical values $n_{SW} = 4$ cm^{-3}, $U_{SW} = 400$ km/s, $T_P = 3.5 \times 10^5$ K, $B_X = -1.6$ nT, and $B_Y = 2.5$ nT (corresponding to the 3 nT Parker spiral

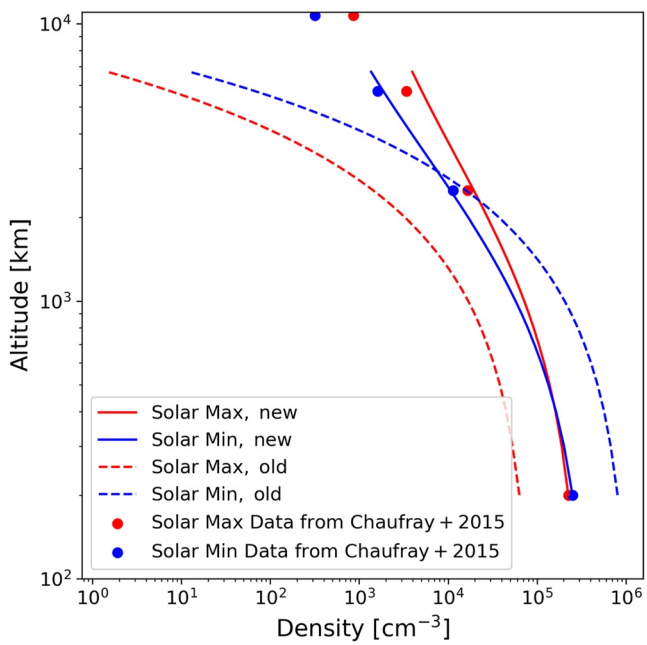

Figure 1. Hydrogen density profiles adopted in this work (solid lines) and in previous works (dashed lines), such as Ma et al. (2004). The seasonal-averaged dayside H density from Chaufray et al. (2015) is shown in red dots (for solar maximum) and blue dots (for solar minimum).

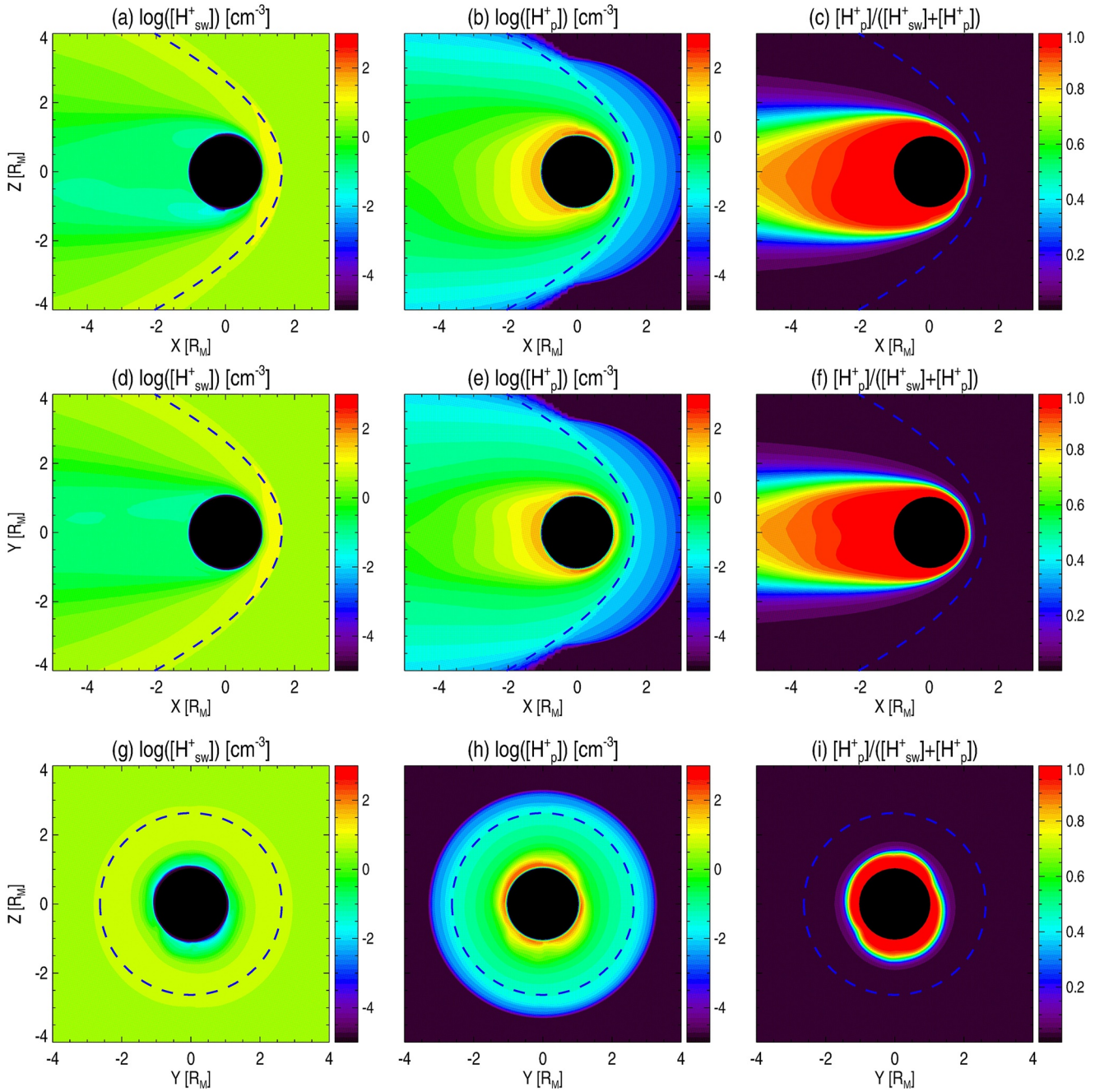

Figure 2. Proton density distributions for Case 1 in (a–c) the *X*–*Z* plane, (d–f) the *X*–*Y* plane, (g–i) the *Y*–*Z* plane. (a), (d), and (g) show the solar wind proton densities. (b), (e), and (h) show the planetary proton densities. (c), (f), and (i) show the ratios of the planetary proton density over the total proton density. Blue dashed lines represent the averaged bow shock location from Trotignon et al. (2006).

magnetic field). Table 2 presents the summary of the key parameters and conditions for each case used in the study, in which Case 1 is the baseline case and any parameters that differ from those used in Case 1 are highlighted in bold.

Table 1 presents the critical parameters and conditions for each case.

Table 2
Cases and Their Key Parameters and Conditions

Cases	Solar EUV conditions	Crustal field	H-O charge exchange	Impact ionization
Case 1	Solar max	Yes	Yes	Yes
Case 2	Solar max	**No**	Yes	Yes
Case 3	Solar max	Yes	**No**	Yes
Case 4	Solar max	Yes	Yes	**No**
Case 5	**Solar min**	Yes	Yes	Yes
Case 6	**Solar min**	Yes	**No**	Yes
Case 7	**Solar min**	Yes	Yes	**No**

3. Results

3.1. The Distributions of Solar Wind Protons and Planetary Ions

First, we compare the results of the 5-species model with the results of the 4-species model to validate the new model. The 5-species model gives identical results as the 4-species model in terms of the total proton densities, heavy ion densities, velocities, pressures, and magnetic fields (not shown) as expected since the separation of solar wind protons and planetary protons does not introduce any new MHD physics. Figure 2 reveals the different distributions of solar wind protons and planetary protons for Case 1 in the *X*–*Z*, *X*–*Y*, and *Y*–*Z* planes, respectively, which is the main purpose of introducing the 5-species model. The blue dashed lines indicate the averaged bow shock location calculated from Phobos-2 and Mars Global Surveyor measurements (Trotignon et al., 2006), showing that our model gives consistent bow shock location especially at low solar zenith angles. Panels 2a, 2d, and 2g show that solar wind protons are piling up inside the bow shock, but strongly depleted in the tail region. The planetary protons beyond the bow shock are noticeable in panels 2b and 2e because the neutral hydrogen is still not negligible at those altitudes as included in our model. However, as shown by the ratio of planetary protons over total protons in panels 2c, 2f, and 2i, planetary protons beyond the bow shock are much less than solar wind protons. The ratio in panel 2i also shows an asymmetry in the *Y*–*Z* plane, with an inclination similar to the tilt of the twisted Martian magnetotail for positive IMF B_Y as observed by MAVEN (DiBraccio et al., 2018). We also examined the location of subsolar ion composition boundary (ICB), defined as the transition layer between planetary ions (H^+_p and heavy ions such as O^+, $O_2{}^+$, $CO_2{}^+$) dominated region and solar wind (H^+_{sw}) dominated region. The subsolar ICB altitude in our model is ~668 km at solar max and ~566 km at solar min. Due the lack of the ability to distinguish H^+_{sw} and H^+_p, in previous works, a practical ICB is normally used, defined as the transition layer between heavy ion (O^+, $O_2{}^+$, $CO_2{}^+$, and so on) to proton (both H^+_{sw} and H^+_p) dominated region. The approximate subsolar ICB in our model is ~563 km at solar max and ~358 km at solar min. The discrepancy between the two definitions of ICB can be over 100 km, suggesting the importance of separating H^+_{sw} and H^+_p. As a comparison, Figure S1 shows that the approximate ICB in our model agrees well with the nominal ICB derived from MAVEN observations (Halekas et al., 2018).

Figure 3a shows ion density distributions and some possibly related factors at 250-km altitude spherical surface for the same baseline Case 1. Densities of H^+_{sw}, H^+_p, O^+, and $O_2{}^+$ are arranged from left to right on the first row. The first panel on the second row shows the radial component of MHD forces (the summation of $J \times B$ force and

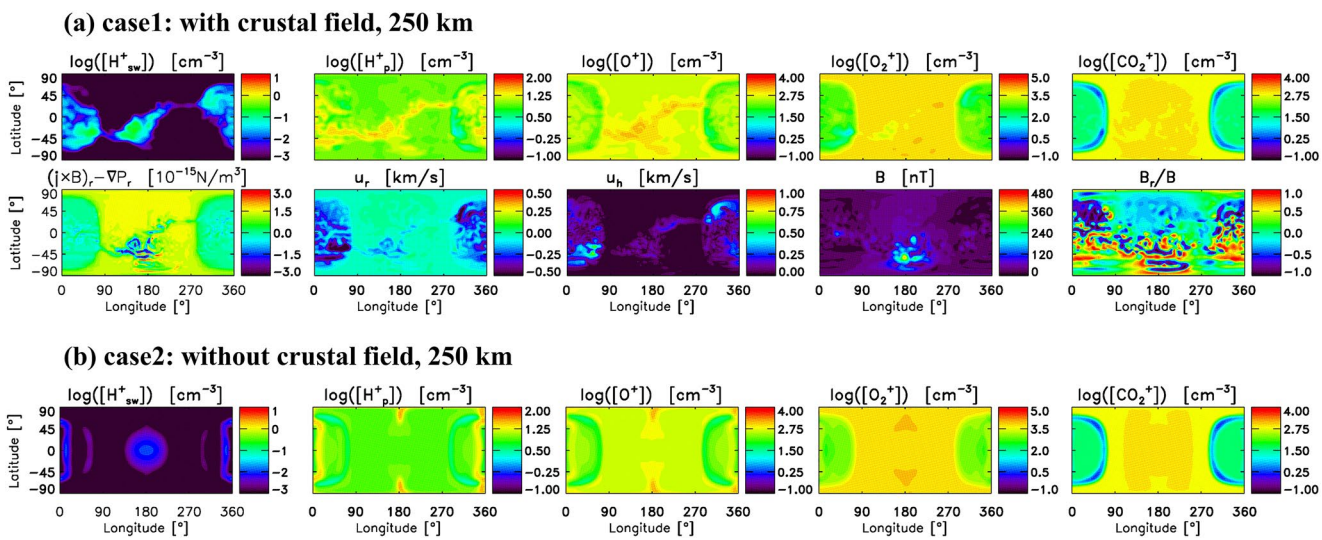

Figure 3. (a) Ion density distributions and related factors at the spherical surface of 250-km altitude, for the case with crustal field (Case 1). (b) Ion density distributions for the case without crustal field (Case 2). Note that the color bars are different for different ion species.

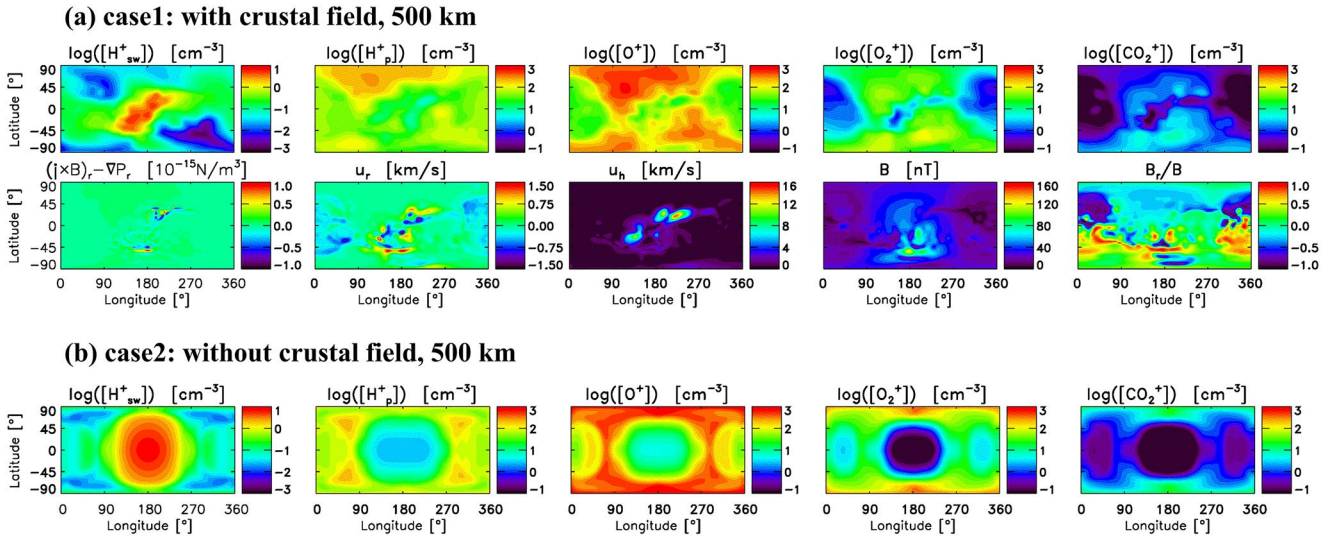

Figure 4. (a) Ion density distributions and related factors at the spherical surface of 500-km altitude, for the case with crustal field (Case 1). (b) Ion density distributions for the case without crustal field (Case 2). Note that the color bars are different from those in Figure 3.

pressure gradient force). The second and third panels on the second row show the radial and horizontal velocity. The last two panels on the second row are magnetic field strength and the ratio of the radial magnetic field over magnetic field strength. To show the influence of the crustal magnetic field on planetary ion distributions and solar wind precipitation at low altitudes, we ran a case without the crustal field (B_c) (Case 2), as shown in Figure 3b. In Figure 3, the subsolar point is located at Lat = 0°, Lon = 180°. The dusk side terminator (+Y-axis in MSO coordinate system) is along Lon = 270°, while the dawn side terminator (−Y-axis in MSO coordinate system) is along Lon = 90°. At 250-km altitude, the O_2^+ ion is by far the most dominant ion species, and planetary protons are much denser than solar wind protons. In Figure 3a, there are clearly tilted solar wind density enhancement regions whose tilt direction is related to the asymmetry in Figure 2i. The shape of the enhanced precipitation region is similar to the region with stronger inward MHD force and inward radial velocity. However, the shape is not directly related to either magnetic field strength, radial component ratio, or the topology (open, draped or closed, not shown) of the magnetic field. This suggests that the effects of magnetic field on plasma are important but complicated. This is because the magnetic field affects the plasma motion through the $J \times B$ force rather than exerting a direct influence. In Figure 3b, the tilted regions disappear in Case 2 due to the absence of a crustal field, which is consistent with the hypothesis proposed by DiBraccio et al. (2018) that the IMF-crustal field interaction may be the main cause of the twisted tail. These low-altitude, dayside features may have a common cause with the twisted magnetotail. We surprisingly find that the case without a crustal field shows less solar wind precipitation at this altitude. This is possibly because the presence of the crustal fields enables localized solar wind precipitation at very low altitudes by adding more radial magnetic field on the dayside.

Figure 4 is in the same format as Figure 3 but at 500-km altitude. At this altitude, O^+ ion is the dominant ion species. Planetary protons are much denser than solar wind protons at most places, except the subsolar region where the ionosphere is mostly compressed by the shocked solar wind. As a result of the compression, the planetary ion densities are relatively low in the subsolar region, with a similar shape to the solar wind density enhancement region. In Figure 4a, the tilts related to twisted magnetotail can still be found. The relation between ion densities and radial velocity at this altitude is not as clear as compared with lower altitude results, because the horizontal velocity is the dominant component of velocity. Comparing Figures 4a and 4b, we find that the case with the crustal field shows less solar wind on the dayside, as expected, due to the shielding effect of the crustal field at this altitude. On the other hand, the densities of planetary ions in the subsolar region for the noncrustal field case are lower due to downward plasma flow which prohibit the diffusion of the planetary ions to this high altitude.

The distributions of solar wind and other ion species are also influenced by other factors such as IMF and solar EUV, which are beyond the scope of this work. Parameter study of solar wind precipitation can be a future utilization of this model. Another thing worthy of being mentioned is that some of the features such as the

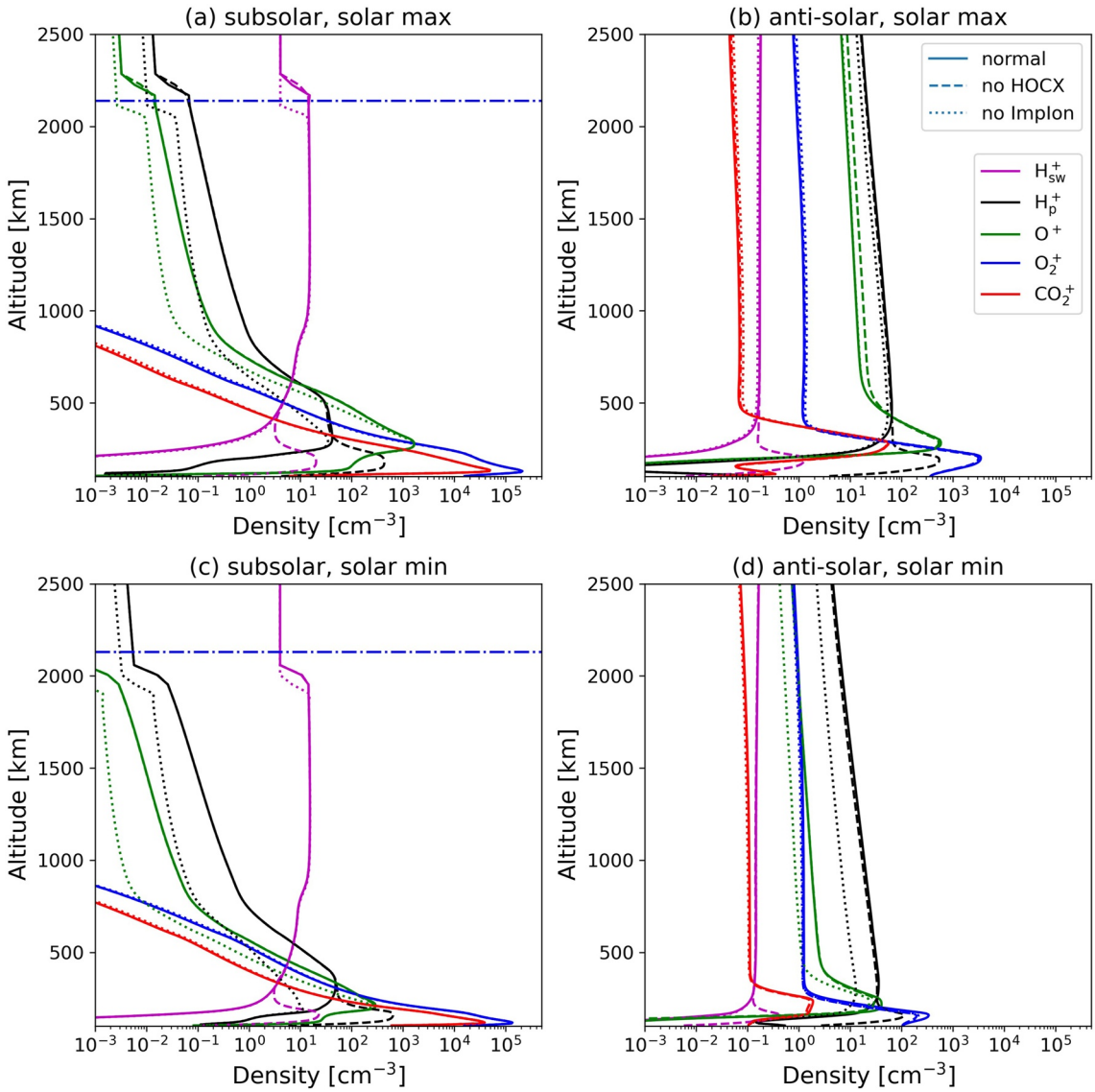

Figure 5. Ion density profiles for (a) subsolar line at solar max, (b) antisolar line at solar max, (c) subsolar line at solar min, (d) antisolar line at solar min. In each panel, there are three sets of ion density profiles: normal case (in solid line), case without HOCX (in dashed line), and case without ImpIon (in dotted line). The horizontal blue dash-dot lines indicate subsolar bow shock location calculated from Trotignon et al. (2006).

correlation between solar wind and planetary ions could be caused by the single-fluid assumption that all ion species share the same velocity. Multifluid models and more low-altitude measurements are required to validate the single-fluid assumption.

3.2. Effects of HOCX and ImpIon

The influences of H-O charge exchange (HOCX) and impact ionization (ImpIon) are investigated with the model. All cases in Sections 3.2 and 3.3 are set with the strong crustal field on the dayside. Figure 5 shows the ion density profiles over 100–2,500 km along the subsolar and antisolar lines, at solar max and solar min, respectively. Each panel includes densities of the normal case with all reactions listed in Table 1 (Case 1/Case 5), the case without HOCX (Case 3/Case 6), and the case without ImpIon (Case 4/Case 7) for comparison. The sharp density jumps in Figures 5a and 5c are caused by the plasma compression across the bow shock into the magnetosheath. The subsolar bow shock location in our model agrees well with previous observations (Trotignon et al., 2006), which are shown in horizontal lines in Figures 5a and 5c. Ion density at high altitudes is hardly affected by HOCX,

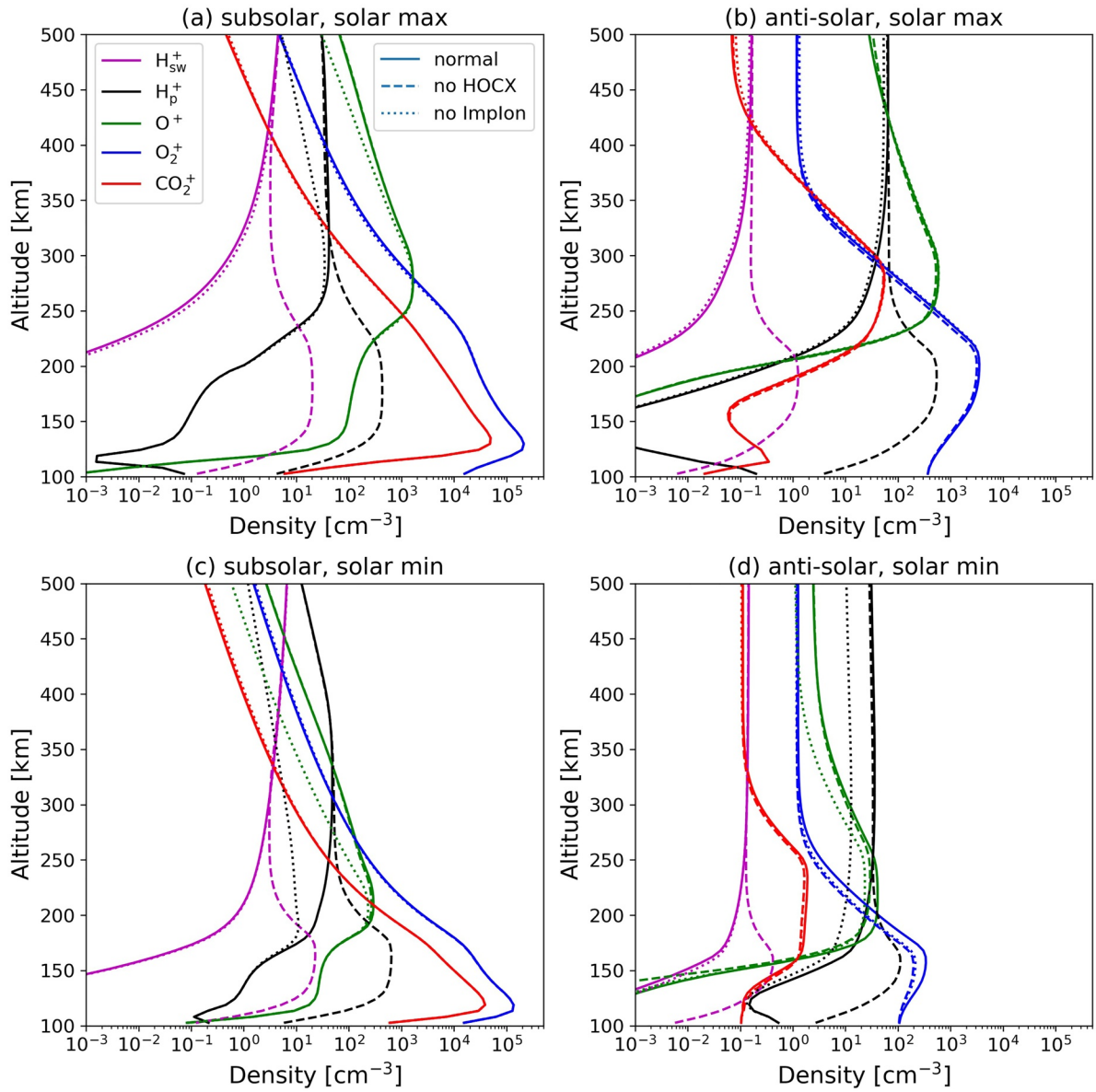

Figure 6. Ion density profiles for lower altitudes. Figure format is the same as Figure 5.

especially in the subsolar region. The most evident difference caused by HOCX at high altitudes is an increase of antisolar O^+ density at solar max. The main effect of switching HOCX off is an accumulation of protons at low altitudes, as there are no other reactions to consuming protons. Impact ionization has a much greater influence at high altitudes. As expected, along subsolar lines, H^+_p and O^+ densities are significantly reduced without impact ionization, while O_2^+ and CO_2^+ densities show no apparent difference. The subsolar bow shock locations are slightly lower when impact ionization is neglected, because there are fewer charged particles to stop the shocked solar wind. However, the penetration depths of solar wind protons do not change appreciably. The densities without ImpIon at nightside are difficult to explain and predict, as the nightside ionosphere is controlled not only by chemical reactions but also by plasma transport. Nevertheless, we still find that the antisolar H^+_p and O^+ densities at solar min are reduced and the antisolar H^+_p density at solar max is slightly reduced.

Given that HOCX mainly influences ion densities at low altitudes, we focus on regions below 500 km in Figure 6 to highlight the differences. Along subsolar lines, HOCX seems to merely influence proton densities. Along antisolar lines, besides the accumulation of protons, panel 6d also shows that heavy ion densities decrease slightly for the cases without HOCX at solar min, while they are almost the same at solar max in panel 6b. Recalling that

Table 3
Integrated Fluxes of All Five Ion Species for Cases Using the New 5-Species Model

Ion species	Solar condition	Escape rate (s^{-1}) (at $6R_M$) Normal case	Without HOCX	Without ImpIon
H^+_{sw}	Max	-2.82×10^{24}	-2.83×10^{24}	-2.53×10^{24}
	Min	-2.28×10^{24}	-2.28×10^{24}	-2.20×10^{24}
H^+_p	Max	1.15×10^{25}	1.12×10^{25}	4.79×10^{24}
	Min	5.81×10^{24}	5.76×10^{24}	1.73×10^{24}
O^+	Max	4.43×10^{24}	4.70×10^{24}	2.89×10^{24}
	Min	9.75×10^{23}	9.99×10^{23}	3.80×10^{23}
O_2^+	Max	4.08×10^{23}	4.01×10^{23}	4.26×10^{23}
	Min	6.02×10^{23}	5.94×10^{23}	6.29×10^{23}
CO_2^+	Max	2.96×10^{22}	2.96×10^{22}	3.26×10^{22}
	Min	6.24×10^{22}	6.23×10^{22}	6.71×10^{22}

Note. A negative flux represents a net inflow to the $6R_M$ sphere.

the most evident difference caused by HOCX at high altitudes is the increase of antisolar O^+ at solar max, it is not clear why the influence of HOCX on antisolar heavy ions at low altitudes seems more important at solar min.

3.3. Integrated Fluxes and Reaction Rates

Escape rates or inflows integrated over a $6R_M$ sphere for different cases are listed in Table 3. Ion fluxes integrated at different surfaces do not vary noticeable beyond $6R_M$. For normal cases at both solar max and solar min, H^+_p loss rates are larger than integrated fluxes of other ions, including the inflow of H^+_{sw}. As mentioned in Section 1, the estimated total atomic H escape rate is $\sim 10^{26\text{–}27}$ s^{-1}. Therefore, the H^+_p escape rates in our model are roughly 1–2 orders less than atomic H escape rates. Heavy ion escape rates show consistent features with previous work (e.g., Ma et al., 2004): O^+ is the most important heavy ion escaping at solar max; O^+ and O_2^+ loss rates are comparable at solar min. Solar activity exerts great influence on planetary ion escape rates, when the solar wind inflow is relatively steady. To quantify the influences of the various reactions on escape rates, Figure 7 shows the escape rates normalized by the normal escape rates. It suggests that impact ionization contributes 30%–70% to H^+_p and O^+ escape rates, for the two solar activity conditions examined. As shown in Figure 5, the effect of HOCX is less important at higher altitudes, therefore also not significant for the escape fluxes, except for O^+ fluxes at solar max.

To better understand the relative importance of each process, Table 4 lists the integrated reaction rates in Case 1 and Case 5 between the inner boundary (100-km altitude) and $3R_M$, which is the whole region where ion chemistry is included in our model. Since CO_2 is the main component of the Martian atmosphere, photoionization of CO_2 is the most important of all ionization processes. The integrated CO_2^+ photoionization rate in the region is between 1×10^{28} and 2×10^{28} depending on solar activity, and is several orders of magnitude larger than the total ion escape rate. Charge exchange reactions between CO_2^+ and O are the major sources of O^+ and O_2^+, which also lead to a quick transformation of CO_2^+. The electron loss process in the model is through the dissociative recombination of CO_2^+ and O_2^+, of which, the recombination of O_2^+ is more important than that of CO_2^+ by a factor of

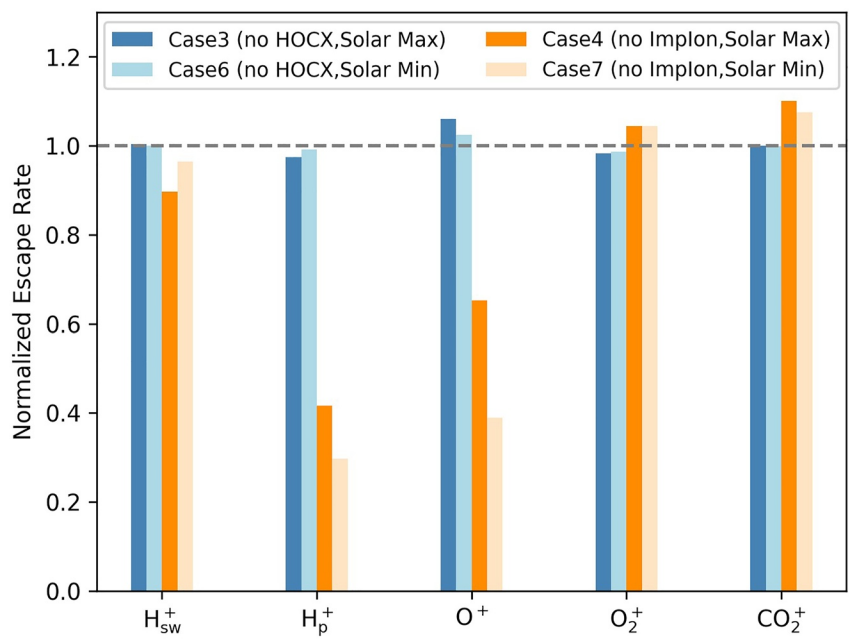

Figure 7. Escape rates normalized by corresponding normal case escape rates.

Table 4
Integrated Reaction Rates in the Model for (a) Solar Max and (b) Solar Min

Ion species	H^+_{sw}	H^+_p	O^+	O_2^+	CO_2^+
(a) Case 1: solar max					
Photon ionization		5.36×10^{24}	4.79×10^{26}		2.18×10^{28}
Impact ionization		6.72×10^{24}	1.86×10^{24}		
$H^+_{sw} + O \rightarrow O^+ + H$	-1.98×10^{22}		1.98×10^{22}		
$H^+_p + O \rightarrow O^+ + H$		-6.42×10^{24}	6.42×10^{24}		
$O^+ + H \rightarrow H^+_p + O$		4.73×10^{24}	-4.73×10^{24}		
$O^+ + CO_2 \rightarrow O_2^+ + CO$			-6.18×10^{27}	6.18×10^{27}	
$CO_2^+ + O \rightarrow O_2^+ + CO$				9.74×10^{27}	-9.74×10^{27}
$CO_2^+ + O \rightarrow O^+ + CO_2$			5.70×10^{27}		-5.70×10^{27}
$O_2^+ + e \rightarrow O + O$				-1.54×10^{28}	
$CO_2^+ + e \rightarrow CO + O$					-6.31×10^{27}
Ion species	H^+_{sw}	H^+_p	O^+	O_2^+	CO_2^+
(b) Case 5: solar min					
Photon ionization		2.73×10^{24}	8.78×10^{25}		1.09×10^{28}
Impact ionization		4.60×10^{24}	1.13×10^{24}		
$H^+_{sw} + O \rightarrow O^+ + H$	-1.36×10^{22}		1.36×10^{22}		
$H^+_p + O \rightarrow O^+ + H$		-3.07×10^{24}	3.07×10^{24}		
$O^+ + H \rightarrow H^+_p + O$		7.66×10^{23}	-7.66×10^{23}		
$O^+ + CO_2 \rightarrow O_2^+ + CO$			-2.90×10^{27}	2.90×10^{27}	
$CO_2^+ + O \rightarrow O_2^+ + CO$				4.80×10^{27}	-4.80×10^{27}
$CO_2^+ + O \rightarrow O^+ + CO_2$			2.81×10^{27}		-2.81×10^{27}
$O_2^+ + e \rightarrow O + O$				-6.26×10^{27}	
$CO_2^+ + e \rightarrow CO + O$					-3.09×10^{27}

Note. A negative (positive) value means this reaction makes the total amount of the corresponding ion density decrease (increase) in the region. The unit is (ions/s).

2.0–2.4. Impact ionization is the governing source of H^+_p. Table 4 suggests that even though impact ionization is not the major source of O^+, it still contributes significantly to the O^+ loss rate. It is probably because impact ionization usually occurs at high altitudes, meaning impact ionized O^+ is easier to be picked up and lost to space.

4. Conclusion

With the 5-species MHD model, we are able to separately analyze the distributions, fluxes, and reactions of solar wind protons and planetary protons of Mars. The global distributions of solar wind and planetary ions at low altitudes are strongly affected by the crustal field. At both solar maximum and minimum, the integrated planetary proton escape rates are larger than the heavy ion escape rates and solar wind proton inflows. The planetary proton escape rate is 1–2 orders less than previously derived atomic hydrogen escape rate. The densities of both types of protons at low altitudes increase significantly if H-O charge exchange is excluded, indicating that H-O charge exchange exerts great influence on proton densities at low altitudes. The loss rate of planetary protons is strongly influenced by impact ionization and solar activity, while the integrated flux of solar wind protons is relatively steady. In addition to the solar activity conditions discussed in this paper, other driving forces, such as solar wind dynamic pressure, IMF, strong crustal field location, etc., should also be investigated in the future to better understand the planetary proton loss process. It is worth noting that the calculated proton escape rates are likely tightly related to neutral hydrogen density, which is now estimated with an atmospheric model and set to be a simplified 1-D profile. In the future, we aim to adopt a more accurate H density, such as a 3-D model based on MAVEN measurements. It is also interesting to investigate proton loss processes with more severe solar wind and solar radiation conditions, which can be related to space weather events, the new solar maximum, and the ancient Mars.

Data Availability Statement

The BATS-R-US code is publicly available online (https://github.com/MSTEM-QUDA/BATS-RUS). The data analyzed in this work are available at the website: https://datadryad.org/stash/share/hYb4o4toUmCANJ_ACTiQCp4JU_2KFy8ztYJafX43ZYU.

Acknowledgments
This work was supported by the NASA Grant NNH10CC04C to the University of Colorado and by subcontract to UCLA. The MAVEN project was supported by the NASA through the Mars Exploration Program. Resources supporting this work were provided by the NASA High-End Computing (HEC) Program through the NASA Advanced Supercomputing (NAS) Division at Ames Research Center.

References

Acuña, M., Connerney, J., Ness, F. N., Lin, R., Mitchell, D., Carlson, C. W., et al. (1999). Global distribution of crustal magnetization discovered by the Mars Global Surveyor MAG/ER Experiment. *Science*, *284*(5415), 790–793. https://doi.org/10.1126/science.284.5415.790

Arkani-Hamed, J. (2001). A 50-degree spherical harmonic model of the magnetic field of Mars. *Journal of Geophysical Research*, *106*(E10), 23197–23208. https://doi.org/10.1029/2000JE001365

Barabash, S., Fedorov, A., Lundin, R., & Sauvaud, J. (2007). Martian atmospheric erosion rates. *Science*, *315*(5811), 501–503. https://doi.org/10.1126/science.1134358

Brain, D., McFadden, J., Halekas, J., Connerney, J., Bougher, S., Curry, S., et al. (2015). The spatial distribution of planetary ion fluxes near Mars observed by MAVEN. *Geophysical Research Letters*, *42*, 9142–9148. https://doi.org/10.1002/2015GL065293

Brecht, S. H., & Ledvina, S. A. (2010). The loss of water from Mars: Numerical results and challenges. *Icarus*, *206*(1), 164–173. https://doi.org/10.1016/j.icarus.2009.04.028

Chaufray, J., Gonzalez-Galindo, F., Forget, F., Lopez-Valverde, M., Leblanc, F., Modolo, R., & Hess, S. (2015). Variability of the hydrogen in the Martian upper atmosphere as simulated by a 3D atmosphere-exosphere coupling. *Icarus*, *245*, 282–294. https://doi.org/10.1016/j.icarus.2014.08.038

DiBraccio, G. A., Luhmann, J. G., Curry, S. M., Espley, J. R., Xu, S., Mitchell, D. L., et al. (2018). The twisted configuration of the Martian magnetotail: Maven Observations. *Geophysical Research Letters*, *45*, 4559–4568. https://doi.org/10.1029/2018GL077251

Dong, C., Bougher, S., Ma, Y., Toth, G., Lee, Y., Nagy, A., et al. (2015). Solar wind interaction with the Martian upper atmosphere: Crustal field orientation, solar cycle, and seasonal variations. *Journal of Geophysical Research: Space Physics*, *120*, 7857–7872. https://doi.org/10.1002/2015JA020990

Dong, C., Ma, Y., Bougher, S., Toth, G., Nagy, A., Halekas, J., et al. (2015). Multifluid MHD study of the solar wind interaction with Mars' upper atmosphere during the 2015 March 8th ICME event. *Geophysical Research Letters*, *42*, 9103–9112. https://doi.org/10.1002/2015GL065944

Dubinin, E., Fraenz, M., Pätzold, M., Woch, J., McFadden, J., Fan, K., et al. (2020). Impact of Martian crustal magnetic field on the ion escape. *Journal of Geophysical Research: Space Physics*, *125*, e2020JA028010. https://doi.org/10.1029/2020JA028010

Dubinin, E., Fraenz, M., Woch, J., Barabash, S., Lundin, R., & Yamauchi, M. (2006). Hydrogen exosphere at Mars: Pickup protons and their acceleration at the bow shock. *Geophysical Research Letters*, *33*, L22103. https://doi.org/10.1029/2006GL027799

Dubinin, E., Lundin, R., Norberg, O., & Pissarenko, N. (1993). Ion acceleration in the Martian tail: Phobos observations. *Journal of Geophysical Research*, *98*(A3), 3991–3997. https://doi.org/10.1029/92JA02233

Ergun, R., Andersson, L., Peterson, W., Brain, D., Delory, G., Mitchell, D., et al. (2006). Role of plasma waves in Mars' atmospheric loss. *Geophysical Research Letters*, *33*, L14103. https://doi.org/10.1029/2006GL025785

Fang, X., Liemohn, M. W., Nagy, A. F., Ma, Y., De Zeeuw, D. L., Kozyra, J. U., & Zurbuchen, T. H. (2008). Pickup oxygen ion velocity space and spatial distribution around Mars. *Journal of Geophysical Research*, *113*, A02210. https://doi.org/10.1029/2007JA012736

Fang, X., Ma, Y., Brain, D., Dong, Y., & Lillis, R. (2015). Control of Mars global atmospheric loss by the continuous rotation of the crustal magnetic field: A time-dependent MHD study. *Journal of Geophysical Research: Space Physics*, *120*, 10926–10944. https://doi.org/10.1002/2015JA021605

Gunell, H., Maggiolo, R., Nilsson, H., Stenberg Wieser, G., Slapak, R., Lindkvist, J., et al. (2018). Why an intrinsic magnetic field does not protect a planet against atmospheric escape. *Astronomy & Astrophysics*, *614*, L3. https://doi.org/10.1051/0004-6361/201832934

Halekas, J. (2017). Seasonal variability of the hydrogen exosphere of Mars. *Journal of Geophysical Research: Planets*, *122*, 901–911. https://doi.org/10.1002/2017JE005306

Halekas, J., & McFadden, J. (2021). Using solar wind helium to probe the structure and seasonal variability of the Martian hydrogen Corona. *Journal of Geophysical Research: Planets*, *126*, e2021JE007049. https://doi.org/10.1029/2021JE007049

Halekas, J. S., McFadden, J. P., Brain, D. A., Luhmann, J. G., DiBraccio, G. A., Connerney, J. E., et al. (2018). Structure and variability of the Martian ion composition boundary layer. *Journal of Geophysical Research: Space Physics*, *123*, 8439–8458. https://doi.org/10.1029/2018JA025866

Harnett, E. M., & Winglee, R. M. (2006). Three-dimensional multifluid simulations of ionospheric loss at Mars from nominal solar wind conditions to magnetic cloud events. *Journal of Geophysical Research*, *111*, A09213. https://doi.org/10.1029/2006JA011724

Jakosky, B., Grebowsky, J., Luhmann, J., & Brain, D. (2015). Initial results from the MAVEN mission to Mars. *Geophysical Research Letters*, *42*, 8791–8802. https://doi.org/10.1002/2015GL065271

Jakosky, B., & Phillips, R. (2001). Mars' volatile and climate history. *Nature*, *412*, 237–244. https://doi.org/10.1038/35084184

Jakosky, B. M., Brain, D., Chaffin, M., Curry, S., Deighan, J., Grebowsky, J., et al. (2018). Loss of the Martian atmosphere to space: Present-day loss rates determined from MAVEN observations and integrated loss through time. *Icarus*, *315*, 146–157. https://doi.org/10.1016/j.icarus.2018.05.030

Ledvina, S., Brecht, S., Brain, D., & Jakosky, B. (2017). Ion escape rates from Mars: Results from hybrid simulations compared to MAVEN observations. *Journal of Geophysical Research: Space Physics*, *122*, 8391–8408. https://doi.org/10.1002/2016JA023521

Lundin, R., Zakharov, A., Pellinen, R., Barabasj, S., Borg, H., Dubinin, E., et al. (1990). Aspera/Phobos measurements of the ion outflow from the MARTIAN ionosphere. *Geophysical Research Letters*, *17*(6), 873–876. https://doi.org/10.1029/GL017i006p00873

Ma, Y., Fang, X., Russell, C. T., Nagy, A., Toth, G., Luhmann, J., et al. (2014). Effects of crustal field rotation on the solar wind plasma interaction with Mars. *Geophysical Research Letters*, *41*, 6563–6569. https://doi.org/10.1002/2014GL060785

Ma, Y., Nagy, A. F., Sokolov, I. V., & Hansen, K. C. (2004). Three-dimensional, multispecies, high spatial resolution MHD studies of the solar wind interaction with Mars. *Journal of Geophysical Research*, *109*, A07211. https://doi.org/10.1029/2003JA010367

Ma, Y., Russell, C. T., Fang, X., Dong, Y., Nagy, A., Toth, G., et al. (2015). MHD model results of solar wind interaction with Mars and comparison with MAVEN plasma observations. *Geophysical Research Letters*, *42*, 9113–9120. https://doi.org/10.1002/2015GL065218

Powell, K., Roe, P., Linde, T., Gombosi, T., & De Zeeuw, D. (1999). A solution-adaptive upwind scheme for ideal magnetohydrodynamics. *Journal of Computational Physics*, *154*(2), 284–309. https://doi.org/10.1006/jcph.1999.6299

Ramstad, R., Barabash, S., Futaana, Y., Nilsson, H., Wang, X., & Holmström, M. (2015). The Martian atmospheric ion escape rate dependence on solar wind and solar EUV conditions: 1. Seven years of Mars express observations. *Journal of Geophysical Research: Planets*, *120*, 1298–1309. https://doi.org/10.1002/2015JE004816

Stone, S., Yelle, R., Benna, M., Lo, D., Elrod, M., & Mahaffy, P. (2020). Hydrogen escape from Mars is driven by seasonal and dust storm transport of water. *Science*, *370*(6518), 824–831. https://doi.org/10.1126/science.aba5229

Tóth, G., van der Holst, B., Sokolov, I. V., De Zeeuw, D. L., Gombosi, T. I., Fang, F., et al. (2012). Adaptive numerical algorithms in space weather modeling. *Journal of Computational Physics*, *231*(3), 870–903. https://doi.org/10.1016/j.jcp.2011.02.006

Trotignon, J., Mazelle, C., Bertucci, C., & Acuña, M. (2006). Martian shock and magnetic pile-up boundary positions and shapes determined from the Phobos 2 and Mars Global Surveyor Data Sets. *Planetary and Space Science*, *54*(4), 357–369. https://doi.org/10.1016/j.pss.2006.01.003